Volume 5
Number 1
7 January 2024
Pages 1–380

Materials Advances

rsc.li/materials-advances

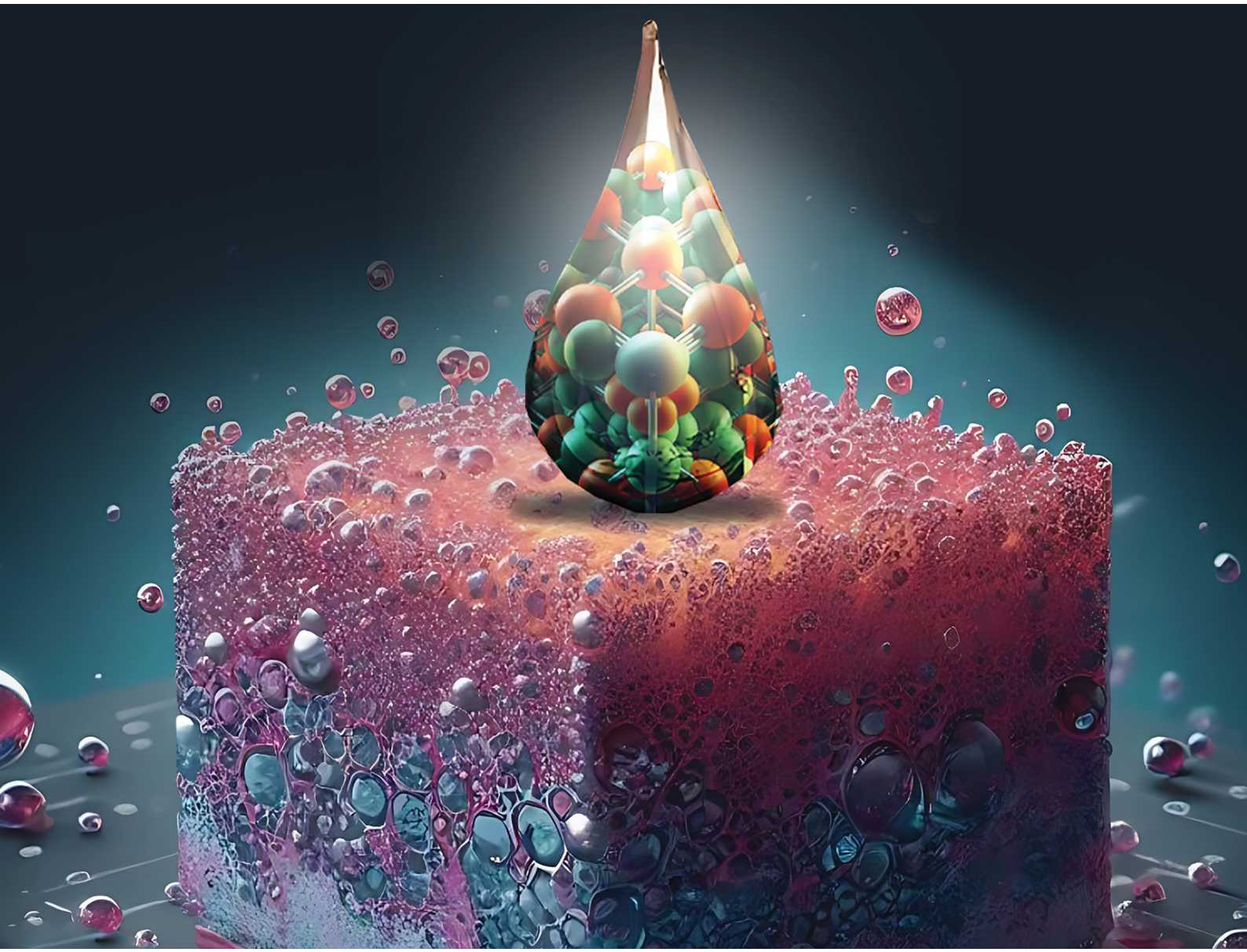

ISSN 2633-5409

ROYAL SOCIETY OF CHEMISTRY

PAPER

Muhammad Imran Asghar *et al.*
A novel $CuFe_2O_4$ ink for the fabrication of low-temperature ceramic fuel cell cathodes through inkjet printing

Materials Advances

ROYAL SOCIETY OF CHEMISTRY

PAPER

View Article Online
View Journal | View Issue

Cite this: *Mater. Adv.*, 2024, 5, 143

A novel $CuFe_2O_4$ ink for the fabrication of low-temperature ceramic fuel cell cathodes through inkjet printing

Sanaz Zarabi Golkhatmi, [a] Peter D. Lund[a] and Muhammad Imran Asghar *[ab]

Inkjet printing is a mask-free, contactless, and precise thin film and coating fabrication technique, which can tailor the electrode microstructure of solid oxide fuel cells to provide a larger surface area with more reaction sites. For the first time, printable and functional $CuFe_2O_4$ inks were developed by analyzing particle size, viscosity, surface tension, density, and thermal properties. Two inks, named Ink (1) and Ink (2), were formulated with different compositions. Ink (2), containing 20 wt% 1,5-pentandiol, exhibited smaller particle sizes (0.87 μm) and a lower activation loss compared to Ink (1). For further optimization, NLK–GDC porous electrolyte substrates were inkjet printed with 30, 40, 50, 100 and 200 layers of Ink (2), with estimated thicknesses of 4.2, 5.6, 7, 14, and 28 μm. The best performance was achieved with a 100-layer inkjet-printed symmetric cell, exhibiting an ASR of 9.91 Ω cm^2. To enhance the rheological properties of Ink (2), cyclopentanone was added, resulting in Ink (2) – Samba, which had improved characteristics. Ink (2) – Samba possessed an average particle size (D50) of 0.68 μm and a *Z* number of 3.89. Finally, EIS analysis compared a 100-layer inkjet-printed symmetric cell with Ink (2) – Samba to a drop-cast cell with the same ink to evaluate how the fabrication technique influences cell performance. Inkjet printing demonstrated a hierarchical porous microstructure, increased reaction sites, and reduced ASR from 19.59 Ω cm^2 to 5.99 Ω cm^2. Additionally, SEM images confirmed that inkjet printing reduced the particle size distribution during deposition. These findings highlight the significant impact of manufacturing techniques on electrode quality and fuel cell electrochemical performance.

Received 2nd July 2023,
Accepted 2nd October 2023

DOI: 10.1039/d3ma00352c

rsc.li/materials-advances

Introduction

Commercialization of solid oxide fuel cell (SOFC) technology often suffers from the high operating temperature (750–1000 °C) necessary to maintain a high enough ionic conductivity to ensure satisfactory performance, which causes material degradation, higher costs, and constraints in materials selection.[1] One way to reduce the operating temperature without sacrificing performance is to develop high-performance materials with engineered microstructures for electrodes, particularly for cathodes, as the oxygen reduction reactions (ORRs) dominate the activation loss in SOFC.[2] Recently, spinel ferrites have gained a lot of interest for different electrochemical devices due to their superparamagnetic characteristics, excellent thermal and chemical stability, and chemical composition.[3] Spinel ferrites with the composition of MFe_2O_4 (M: Mn, Co, Cu, Ni, Mg, *etc.* in octahedral sites) have demonstrated a higher catalytic activity than single-component metal oxides.[4] Furthermore, these spinel oxides have a suitable thermal expansion coefficient (TEC) with the other components, unlike other perovskite materials for SOFC cathodes such as LSCF.[5] Copper ferrite ($CuFe_2O_4$) is a prominent spinel ferrite due to its electrical conductivity and high electrochemical activity.[6] $CuFe_2O_4$ has been used in many applications, including wastewater treatment,[7,8] sensors,[9–11] Li-ion batteries,[12,13] supercapacitors,[14–16] SOFCs,[17–19] and photocatalysts,[20–22] showing positive effects in surface reactions. Inkjet printing, which is an additive manufacturing technique, can tailor the $CuFe_2O_4$ microstructure.[23] It is an efficient, mask-free, contactless, and precise fabrication method for thin films and coating preparation also producing less by-products and waste.[24,25] The formation of single droplets released from a nozzle makes inkjet printing a precise and reproducible film preparation method.[26] Solid oxide fuel cells (SOFCs),[27–30] batteries,[31–33] supercapacitors,[34–36] solar cells,[37–39] and sensors[40–42] have recently benefited from this deposition technique using colloidal suspensions as inks on different substrates by obtaining high-precision and uniform electrode layers with a higher specific surface area.[28] Inkjet printing could maximize the $CuFe_2O_4$ potential in surface reactions by

[a] *New Energy Technologies Group, Department of Applied Physics, Aalto University School of Science, P. O. Box 15100, FI-00076 Aalto, Finland. E-mail: imran.asghar@aalto.fi*
[b] *Renewable Energy Technologies Group, Faculty of Engineering and Natural Sciences, Tampere University, FI-33014, Finland*

depositing a porous and highly structured thin film and providing more active sites for $CuFe_2O_4$ particles.[43] However, $CuFe_2O_4$ ink development for inkjet printing techniques has not yet been reported. Here we develop three $CuFe_2O_4$ inks with different dispersant wt% to work as functional ink in inkjet-printing applications. We studied their particle size distribution, rheological properties, and optimized the printing conditions by adjusting the number of printed layers for SOFC. Finally, the effect of the fabrication technique on SOFC performance was investigated by comparing drop-cast and inkjet-printed $CuFe_2O_4$ symmetric cells *via* electrochemical impedance spectroscopy, Brunauer–Emmett–Teller (BET) analysis, and electron microscopy analysis to determine the impact of inkjet-printing on the microstructural development of the $CuFe_2O_4$ ink. A full fuel cell is also demonstrated for anode-supported 100-layer inkjet-printed and drop-casted complete cells. Current–voltage measurements were carried out to illustrate the functionality of a complete fuel cell consisting of 100-layer inkjet-printed and drop-cast anode-supported cells with Ink (2) – Samba.

Experimental

Cathode inks

The preparation procedure for the inks. The solid composition of the cathode inks was commercially available $CuFe_2O_4$ (Ningbo Sofcman Co. Ltd, China) with an average particle size of 3 μm and a purity of 3 N. The dispersing medium was Terpineol (Sigma-Aldrich, Germany). Ethyl cellulose (EC) and 1,5-pentandiol (both from Sigma-Aldrich, Germany) were used as the dispersant and humectant/surfactant, respectively. Three distinct dispersions with 3.5 wt% $CuFe_2O_4$, 0.03 wt% EC, and three different values of 1,5-pentandiol, including 0 wt%, 15 wt%, and 20 wt%, were prepared to investigate the effect of 1,5-pentandiol on $CuFe_2O_4$ ink printability and electrochemical performance; these inks shall thereafter be known as Ink (0), Ink (1), and Ink (2). The procedure was followed by ball-milling with small, medium, and large zirconia beads in a zirconia jar for 2 weeks at 300 rpm. Finally, the inks were vacuum filtered through glass microfiber filters (Grade GF/B, Whatman). It is worth mentioning that Ink (0) showed poor flow through the vacuum filtration, which was impossible to filter. Ink (2) was then modified for the Samba cartridge to reduce the viscosity with the addition of cyclopentanone (Sigma-Aldrich, Germany) in a volume ratio of 3 : 1 (Ink (2): Cyclopentanone), and named Ink (2) – Samba.

Characterization methods. The inks' particle size distribution was determined using a particle size analyzer (Nanoptic 90, 3P Instruments GmbH & Co. Kg, Germany) based on dynamic light scattering (DLS) theory. Viscosity measurements were performed in a temperature range of 35–70 °C to determine the suitable printing range for the inks using a vibrating viscometer (SV-10, A&D Company, Japan). After finding the appropriate temperature range (40–50 °C) based on the inkjet printer requirements, surface tension measurements were performed using a force tensiometer (Sigma 700, Biolin Scientific, Finland) with a micro roughened surface Platinum Wilhelmy plate. The same instrument and density probe were used to perform the density measurements.

The printability of Ink (1) and Ink (2) was determined by calculating their Reynolds (Re), Weber (We), Ohnesorge (Oh), and Fromm (Z) numbers, then combined in a graphical map by Derby,[44] as given below:[45]

$$\mathrm{Re} = \frac{v\rho\alpha}{\eta} \quad (1)$$

$$\mathrm{We} = \frac{v^2\rho\alpha}{\sigma} \quad (2)$$

$$Z = \mathrm{Oh}^{-1} = \frac{\mathrm{Re}}{\sqrt{\mathrm{We}}} = \frac{\sqrt{\sigma\rho\alpha}}{\eta} \quad (3)$$

where v is the drop velocity (m s^{-1}), ρ is the density (g cm^{-3}), and α is the characteristic length (m), often proportional to the cartridge nozzle diameter (21.5 μm), η is the viscosity (Pa s), and σ is the surface tension (N m^{-1}).

To study the sintering behavior of Ink (1) and Ink (2), thermal examination (TGA/DSC) was performed up to 650 °C at a heating rate of 5 °C min^{-1} under an air atmosphere using a NEXTA STA thermal analyzer (Hitachi, Japan).

Electrolyte substrates

Powder preparation. As the nanocomposite electrolyte substrate was designed with a three-layer structure (porous–dense–porous), two types of NLK–GDC powder were prepared for the dense and porous layers. The electrolyte's porous structure serves as capillary forces, which regulate the stage of drop dispersal and prevent the coffee-string effect.[30,46] The NLK–GDC nanocomposite electrolyte powder for the dense layer was prepared *via* a solid-state ball-milling procedure. Lithium, sodium, and potassium carbonates (Purum, 99%, Sigma-Aldrich, Germany) with a eutectic weight proportion of Li : Na : K = 32.1 : 33.4 : 34.5, were used for the carbonate composition. Then, the eutectic carbonate composition and GDC (WuXi Kai-star Electro-optic Materials Co., China) powders with a 30 : 70 wt% ratio were ball-milled together for 24 h at 300 rpm with zirconia beads. The NLK–GDC nanocomposite powder for the porous layer was formulated with the as-prepared NLK–GDC nanocomposite powder, and 25 wt% EC was added to the mixture, followed by grinding.

Porous substrate preparation. The three-layered porous electrolyte substrates were fabricated by cold pressing a 13 mm die, filled with 0.1 g porous, 0.3 g dense, and 0.1 g porous NLK–GDC powders, for 120 s under a pressing pressure of 250 MPa. Finally, the green-pressed porous pellets were sintered in a muffle furnace (Nabertherm, Germany) at 1 °C min^{-1} up to 350 °C. Then, the sintering was continued at 2 °C min^{-1} to 700 °C. After 1 h maintaining the temperature at 700 °C, the heating profile was completed in a slow cooling step at 1 °C min^{-1} until reaching room temperature. The diameter and thickness of the resulting substrate were 12.2 mm and

1.22 mm, respectively. The substrate consists of a dense layer (0.73 mm) with porous layers (0.25 mm each) on both sides.

Anode-supported substrates

Powder preparation. The anode powder was prepared through a solid-state route. Ni(III) oxide green (99%, Sigma-Aldrich, Germany) and GDC (WuXi Kai-star Electro-optic Materials Co., China) were mixed with a weight ratio of NiO : GDC = 60 : 40 to make NiO-GDC. Then, EC (Sigma-Aldrich, Germany) was added to the NiO-GDC mixture in a weight ratio of NiO-GDC : EC = 90 : 10. The final composition was ball-milled for 1 h at 300 rpm with zirconia beads.

Substrate preparation. The two-layered anode-supported substrates were prepared by cold co-pressing using a 13 mm die, filled with 0.4 g NiO-GDC and 0.3 g GDC, respectively, for 120 s under a 250 MPa pressure. Finally, the green anode-supported substrates were sintered at 1500 °C with a heating rate of 1 °C min^{-1} for 4 h, followed by a cooling step with the same rate until reaching the room temperature.

Fabrication and characterization of symmetric and full fuel cells

Inkjet-printed symmetric cell. A Dimatix DMP-2800 (Fujifilm, Santa Clara, USA) inkjet printer with a piezoelectric transducer and 10 pL Legacy DMP and Samba cartridges was used for the inkjet printing of the porous NLK–GDC nanocomposite electrolytes. The Legacy DMP and Samba cartridges featured 16 and 12 nozzles of 21.5 μm diameter, respectively, and a reservoir with a 1.5 mL capacity. The electrical signal that drives the piezoelectric actuators in the printhead nozzles was controlled by a single waveform with a cartridge temperature of 45 °C, jetting voltage of 35 V, jetting frequency of 30 kHz, and dwell and falling times of 4 and 20 μs, respectively. There was a 10 s delay between printing each layer, and the printer vacuum platen was active. At first, porous NLK–GDC nanocomposite electrolytes were inkjet-printed with 50 layers of Ink (1) and Ink (2) to find the best 1,5-pentandiol wt% for the $CuFe_2O_4$ ink. Once one side was printed, the cell was oven-dried for 1 h at 130 °C before being sintered at 600 °C for 1 h at 1 C min^{-1}. The other side of the cell was printed, dried, and sintered similarly. After determining the appropriate ink composition for $CuFe_2O_4$, Ink (2), it was used to optimize the number of inkjet-printed layers by printing in 30, 40, 50, 100, and 200 layers. Finally, Ink (2) – Samba was inkjet-printed in 100 layers, the optimized number of layers. All the inkjet-printing processes followed the same as-mentioned steps. The ink loading for one side of the 100-layer inkjet-printed cell with Ink (2) – Samba before and after sintering was 10.8 mg and 1.6 mg, respectively.

Drop-cast symmetric cells. Symmetric cells were fabricated using Ink (2) and Ink (2) – Samba and the drop-casting deposition technique to evaluate and compare the electrochemical performance of the optimized inkjet-printed cell. The drop-casting was performed on a hot plate at 60 °C with 0.05 mL of ink through a micropipette on one side of the porous NLK–GDC electrolyte. The drying and sintering steps were done similarly to the inkjet-printed cells. The other side of the drop-cast cell was then drop-cast, dried, and sintered using the same procedure. Concerning the loading of the cells, the objective was to test both inkjet-printed and drop-cast samples with the same loading of the cathode ink. However, some difficulties were encountered in attaining a uniform and homogenous coating through the drop-casting method with the same loading as the inkjet-printed cell. The minimum amount of ink to obtain a homogenous coverage was 0.05 mL, equal to 49.5 mg before sintering. The final loading of one side of the drop-cast sample after sintering was 4.9 mg.

Considering the substrate's thickness, the presence of a porous structure poses challenges in accurately determining the thickness of the ink layer that has been applied. Furthermore, measuring the thickness of the drop-cast cell is a significant challenge due to the non-uniform characteristics of the deposited layer, hence adding complexity to the direct measurement techniques. However, it is possible to approximate the thickness by considering the surface area of the substrate and the density of the ink as below:

$$\rho = \frac{m}{S \times h} \tag{4}$$

where ρ is the ink density (g cm^{-3}), which is 0.99 g cm^{-3}, m is the loading (g), S is the surface area of the cell (cm^2), which is 1.09 cm^2, and h is the thickness of the deposited layer on one side (cm). The estimated thickness of the 100-layer inkjet-printed and drop-cast samples were 14 and 45 μm, respectively.

Inkjet-printed full solid oxide fuel cells. The same process as for the symmetric cells was conducted with anode-supported substrates and Ink (2) – Samba to fabricate 100-layer inkjet-printed complete solid oxide fuel cells.

Drop-cast full solid oxide fuel cells. The fabrication of drop-cast full solid oxide fuel cells was carried out using anode-supported substrates and Ink (2) – Samba, following a similar procedure to that of symmetric cells.

Microstructural characterization. Scanning electron microscopy (SEM) analysis of the optimized inkjet-printed and drop-cast symmetric cells was performed with a Zeiss Sigma VP SEM to study the role of surface morphology in the cell's electrochemical performance. Moreover, samples were investigated by nitrogen gas adsorption–desorption at −196.15 °C (77 K) using BELsorp MAX II (Microtrac BEL, Japan) equipment. A Brunauer–Emmett–Teller (BET) analysis was applied to the results of selected samples to estimate their specific surface area and porosity. All samples were pretreated under vacuum at 160 °C for 4 hours before measurement.

Electrochemical characterization. Electrochemical impedance spectroscopy (EIS) was conducted using a Probostat (NorECs Ltd, Norway) and a Zahner Im6 potentiostat over a frequency range of 100 mHz to 100 kHz open circuit voltage (OCV) and a 20 mV AC amplitude. The temperature range of the measurements was 400–550 °C with 50 °C intervals. The effective surface area of the cell was 0.64 cm^2. To provide reliable electrical contacts during the measurements, Au paste (Metalor, UK) was applied to both sides of the cells and dried in the oven at 200 °C for 2 h beforehand. Gold meshes (NorECs Ltd, Norway) were utilized as current collectors.

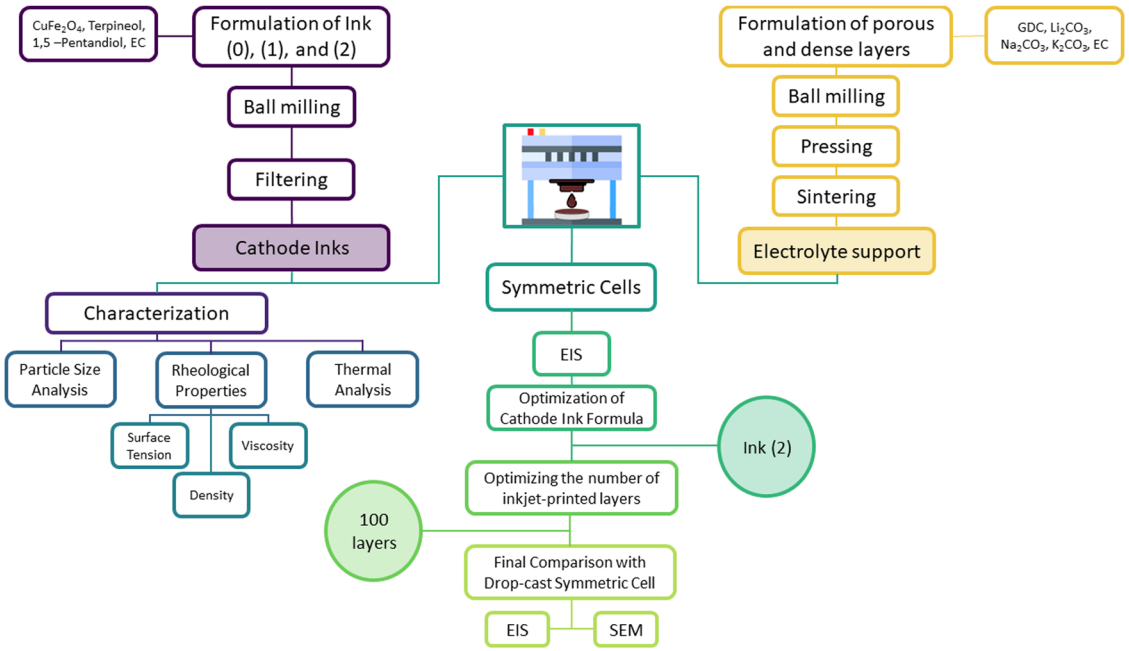

Fig. 1 Experimental steps of fabrication, characterization, and optimization for an inkjet-printed $CuFe_2O_4$ symmetric cell.

Current–voltage (*I–V*) measurements were conducted using the same equipment over a potential range of −1.2 to 1.2 V under open circuit voltage (OCV) conditions and a 20 mV AC amplitude. The temperature range of the measurements was 500–650 °C with 50 °C intervals. The provided gas atmospheres for the anode and cathode were H_2 in the inner chamber with a flow rate of 5 l min^{-1}, and air in the outer chamber with a flow rate of 12.5 l min^{-1}, respectively. The effective surface area of the cell was 0.5 cm^2. Samples were sealed using Ceramabond 552 (Aremco, USA) to avoid gas mixture between the chambers of the Probostat.

The flowchart in Fig. 1 depicts the experimental steps for fabricating, characterizing, and optimizing an inkjet-printed $CuFe_2O_4$ symmetric cell.

Result and discussion

Inks properties

Particle size distribution. An appropriate particle size distribution is crucial to prevent nozzle clogging during inkjet printing, meaning that the largest particles should be less than 10% of the cartridge nozzle size.[47] Nevertheless, too small particles tend to agglomerate due to the high attraction forces (van der Waals) among them causing nozzle blockage.[48] Thus, appropriate dispersant type and quantity are vital to avoid nozzle clogging. Particle size distribution of Ink (0), Ink (1) – prior to filter, Ink (2) – prior to filter, Ink (1), Ink (2), and Ink (2) – Samba are shown in Fig. 2(a). Ink (0) has an average particle size (D50) of 3.59 μm, higher than 10% of 21.5 μm. Moreover, it was impossible to filter the Ink (0) due to the strong sedimentation and filter blockage, confirming the importance of using an appropriate dispersant. In this regard, 1,5-pentandiol is used as a surfactant to prevent agglomeration by creating a steric hindrance effect and stabilizing the particles in the liquid medium.[49] Ink (1) – prior to filter, showed good dispersing behavior and was easily vacuum filtered. However, it has a D50 of 3.63 μm with a secondary peak. After the vacuum filtering of Ink (1), the D50 is lowered to 1.26 μm, lower than the recommended particle size. But still, it has a secondary peak which might cause nozzle clogging issues after a while.[50] Ink (2) – prior to filter D50 is 2.70 μm, smaller than that of Ink (0) and Ink (1), evincing that the dispersant is improving the particle size distribution.[51] After filtration, Ink (1) shows a D50 of 1.26 μm, making it a potential candidate for printable ink, although the secondary peak still exists. Ink (2) has a narrow particle size distribution and an average particle size of 0.87 μm without any secondary peaks, signifying no agglomeration in Ink (2). The addition of cyclopentanone reduced the D50 to 0.68 μm, showing that cyclopentanone can act as an appropriate dispersant in the polar medium of Terpineol and 1,5 – pentandiol.[52] These features can ensure a smooth inkjet printing process without any nozzle clogging.

Rheological properties. The ink printability requires specific rheological properties, such as its viscosity and surface tension, as well as other parameters like drop velocity and density.[53] The viscosity of ceramic ink has a considerable impact on its ejection behavior. A low viscosity is preferable (typically <50 mPa s) for the inkjet printing technique, which restricts the types and amount of used polymer additives in the ink composition.[30] Moreover, it limits the amount of ceramic content in the formulation to provide low-viscosity ink. The ink's viscosity should be adjusted as higher viscosity can cause insufficient jetting. In contrast, too low viscosity may greatly

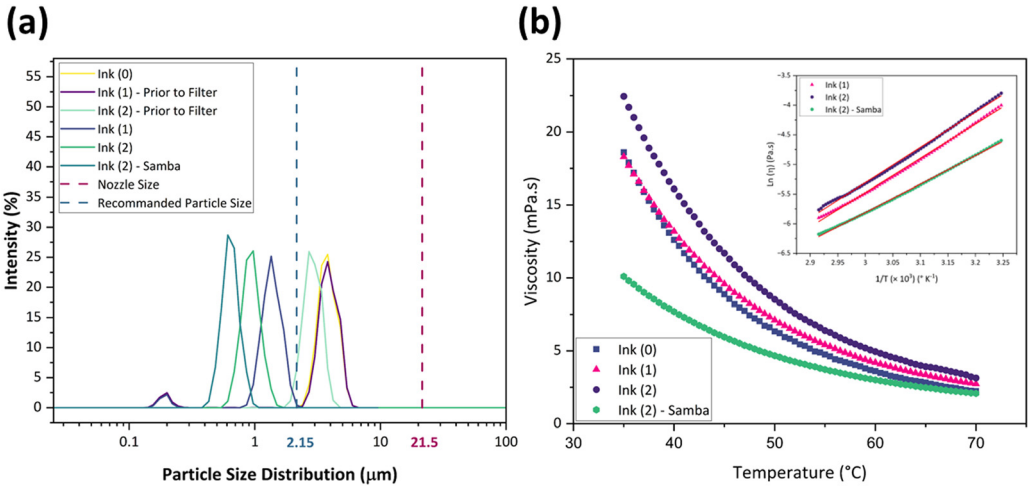

Fig. 2 (a) Particle size distribution of Ink (0), Ink (1) – prior to filter, Ink (2) – prior to filter, Ink (1), Ink (2), and Ink (2) – Samba with average particle sizes of 3.56, 3.63, 2.70, 1.26, 0.87, and 0.68 μm. The cartridge nozzle size and the recommended particle size are also shown in the plot. (b) Viscosity *vs.* temperature plot for Ink (0), Ink (1), Ink (2), and Ink (2) – Samba in the temperature range of 70–35 °C. The inset is the Arrhenius plot for Ink (1), Ink (2), and Ink (2) – Samba, which are practically printable to study the effect of 1,5-pentandiol on viscosity.

reduce friction and end in damped oscillation, significantly impacting jetting speed.[54] In this work, $CuFe_2O_4$ inks were formulated with a low solid content (0.60 vol%) to ensure a low viscosity behavior. Regarding selecting appropriate additives, 1,5-pentandiol is a polyol with hydroxyl (–OH) groups which may create hydrogen bonds with other ink components, such as solvent, and increase the viscosity.[55] An appropriate concentration of 1,5-pentandiol is crucial for the optimum value of the ink's viscosity. Higher concentrations of this surfactant can result in more intermolecular interactions and hence, higher viscosity. Depending on the concentration, this increase in viscosity might be beneficial or harmful to inkjet printing. Fig. 2(b) displays the viscosity plots for Ink (0), Ink (1), and Ink (2) from 70 to 35 °C to determine the optimal printing temperature and study the effect of 1,5-pentandiol on viscosity. The viscosity plot for Ink (2) – Samba is also included in Fig. 2(b). In the viscosity *vs.* temperature plot for all the ink in Fig. 2(b), Ink (2) had the highest viscosity. In contrast, Ink (0) and Ink (1) have close viscosity values, showing that the 15 wt% concentration does not strongly affect changing the viscosity. To provide a better understanding of the 1,5-pentandiol concentration effect on attractive interactions, Arrhenius expression in logarithmic form is used,[56–58] and the plot is shown in Fig. 2(b) inset:

$$\ln(\eta) = \ln(A) + \frac{E_a}{RT} \quad (5)$$

The values of E_a for Ink (1) and Ink (2) were 48.09 and 49.41 kJ, respectively, based on the slope of the fitted line and eqn (5). The E_a values indicate that the hydrogen bonding between 1,5-pentandiol and terpineol hydroxyl groups is getting stronger by increasing the 1,5-pentandiol concentration from 15 wt% to 20 wt%, leading to a higher viscosity.[56,59] Considering the required viscosity range of DMP cartridges (10–12 mPa s), the printing temperature was chosen as 45 °C. The viscosity values of Ink (0), Ink (1), and Ink (2) at 45 °C are 8.87, 9.58, and 11.7 mPa s, respectively. As the range of viscosity requirements is different for the Samba cartridge (4–8 mPa s), Ink (2) was modified to Ink (2) – Samba by using cyclopentanone to alter the viscosity to 5.95 mPa s at 45 °C.[60] The lower E_a (39.83 kJ) and viscosity values for Ink (2) – Samba demonstrate that the addition of cyclopentanone changes the strong intermolecular interactions, including hydrogen bonding and van der Waals forces, between the Terpineol and 1,5-pentandiol molecules, which contribute to the viscosity of the ink and lower it.[61] As cyclopentanone has weaker intermolecular bonds, it could be capable of hindering the formation of strong intermolecular networks, resulting in a decrease in viscosity. Weaker hydrogen bonding interactions may result in fewer molecular entanglements and less resistance to flow, both of which contribute to lower viscosity.[62] Moreover, the smaller particle size can lead to lower viscosity.[63]

Also, the ink's surface tension must be regulated to guarantee the ink wets the channel and ejects from the nozzle.[64] Furthermore, controlled surface tension can prevent the ink from leaking from the nozzle during the no-jetting phase.[64] Fig. 3(a) represents the surface tension values at 45 °C as 27.9, 24.66, 28.43, and 25.53 mN m^{-1} for Ink (0), Ink (1), Ink (2), and Ink (2) – Samba, respectively. These values show that adding 15 wt% 1,5-pentandiol to Ink (0) leads to a decrement in the surface tension due to its lower surface tension value compared to Terpineol. However, adding 20 wt% results in an increase due to the higher attractive intermolecular forces between the solute and the solvent.[56] Also, the ink surface tension is decreased when cyclopentanone is added because of its lower surface tension compared to Terpineol and 1,5-pentandiol.

The rheological specification of a printable ink is determined by the dimensionless numbers in fluid mechanics, including We, Re, Oh, and Fromm numbers. The optimal range of these characteristics has been identified through various research studies. As an example, Fromm[65] proposed $Z > 2$ for consistent drop formation, while Derby[66] determined $1 < Z < 10$.

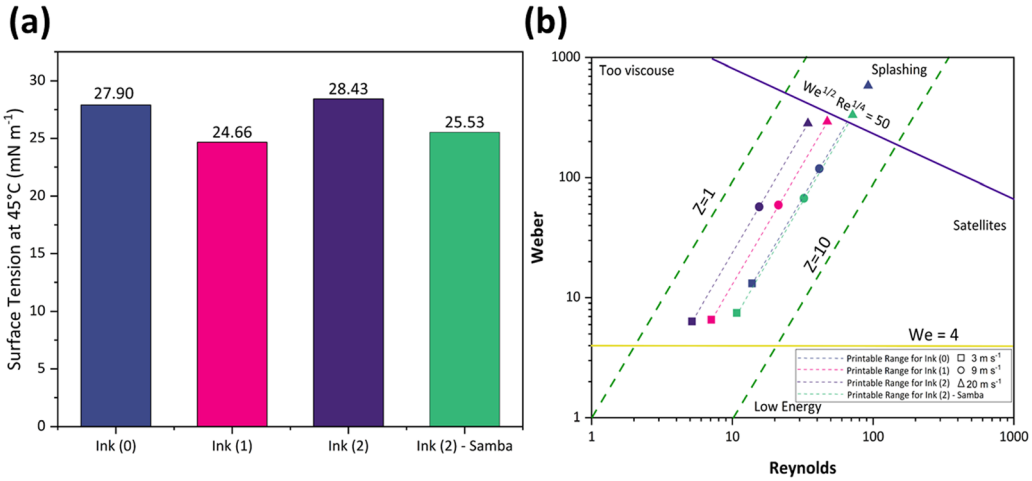

Fig. 3 Ink characterization plots. (a) Surface tension measurement of Ink (0), Ink (1), Ink (2), and Ink (2) – Samba at the printing temperature (45 °C). (b) Derby diagram for Ink (0), Ink (1), Ink (2), and Ink (2) – Samba at the printing temperature (45 °C).

Table 1 Particle size and rheological properties of Ink (0), Ink (1), Ink (2), and Ink (2) – Samba at 45 °C

	Particle size and rheological properties at 45 °C								
Inks	Average particle size (μm)	Viscosity (mPa s)	Surface tension (mN m^{-1})	Density (g cm^{-3})	Oh	Z	Drop velocity (m s^{-1})	We	Re
Ink (0)	3.59	8.89	27.90	1.90	0.26	3.80	9	118.59	41.44
Ink (1)	1.26	9.58	24.66	0.938	0.42	2.32	9	66.27	18.95
Ink (2)	0.87	11.7	28.43	0.936	0.48	2.04	9	57.34	15.48
Ink (2) – Samba	0.68	5.95	25.53	0.99	0.25	3.89	9	67.53	32.19

Considering the rheological requirements for printable ink, Derby created a cartesian map based on Re and We dimensionless numbers to specify the ink characteristics in DoD inkjet systems.[44] Fig. 3(b) depicts the Derby diagram for all the inks with a drop velocity range of 3–20 m s^{-1}. It is worth mentioning that Ink (0) is theoretically printable. However, due to the large particle size and heavy sedimentation, it wasn't used for inkjet printing to avoid nozzle clogging. It can be concluded that particle size distribution is as important as the rheological properties to ensure a good-quality inkjet printing process. Ink properties for all the inks are described in Table 1.

Thermal analysis TGA and DSC analyses were performed for Ink (1) and Ink (2) in the air to study their sintering behavior and the thermal decomposition of solvent remnants and organic components. As the cyclopentanone evaporates at 130 °C and the samples go through a drying step at 130 °C for 1 h, the as-dried Ink (2) – Samba will follow the Ink (2) thermal profile.[60] Fig. 4(a) and (b) exhibit the thermal analysis curves for Ink (1) and Ink (2), respectively. According to TGA curves, there were no weight changes under 100 °C, indicating that the inks' organic medium preserves its weight at room temperature, which is considered a beneficial behavior for long-term storage and stability of the ink.[67] The first and most significant weight loss happened at 100–200 °C, accompanied by endothermic peaks at 177 °C and 185 °C for Ink (1) and Ink (2), respectively. This weight loss is attributable to the degradation of the major amount of organic substances and water evaporation.[68,69] The second weight loss for Ink (1) occurred at 185–210 °C with an endothermic peak at 209 °C, and for Ink (2) happened at 195–210 °C with the same endothermic peak temperature as Ink (1). The thermal breakdown of the residual organic components, organic solvent volatilization, and EC melting all contribute to these endothermic peaks.[30,70,71] After raising the temperature to 400 °C, the remaining organic material was burnt away, and a third endothermic reaction occurred at 414 and 418 °C for Ink (1) and Ink (2), respectively.[30,72] At temperatures over 400 °C, the masses of the inks remained constant. However, there was a fourth endothermic reaction, at 471 °C for Ink (1) and 464 °C for Ink (2), resulting from the $CuFe_2O_4$ phase transition from tetragonal to cubic phase.[73] The total mass loss for Ink (1) was 87.24%, which is lower than that of Ink (2) (93.76%), as Ink (1) had a lower amount of organic substances.

Electrochemical characterization

1,5-Pentandiol wt% optimization. EIS is a helpful technique to study different electrochemical processes involved in a fuel cell, including ionic and electronic transfer (Ohmic losses), and charge transport activation (kinetic losses).[30,74] To determine the best $CuFe_2O_4$ ink formula for the ceramic fuel cell application, 50 layers of inkjet-printed symmetric cells with Ink (1) and Ink (2) were examined using EIS. Fig. 5(a) shows the Nyquist plot for these inkjet-printed symmetric cells at 550 °C. Four distinct sections are seen in these Nyquist plots: a long tail at

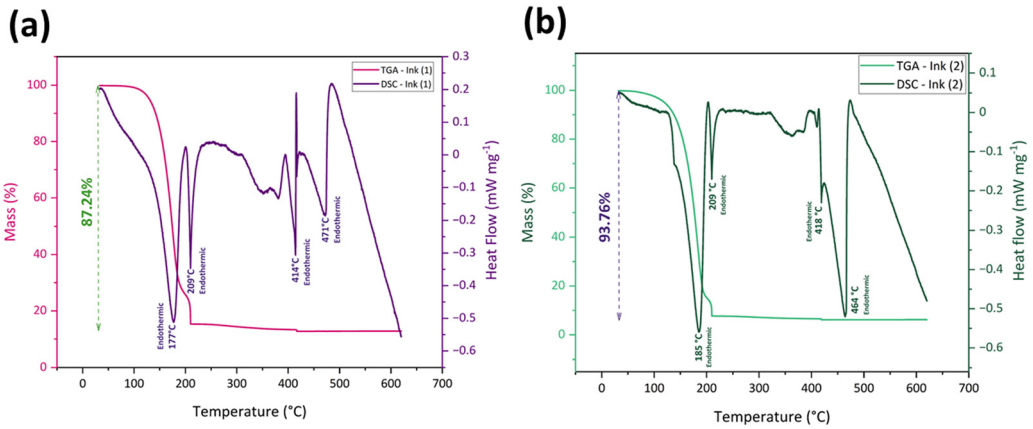

Fig. 4 TGA/DSC curves of (a) Ink (1) and (b) Ink (2).

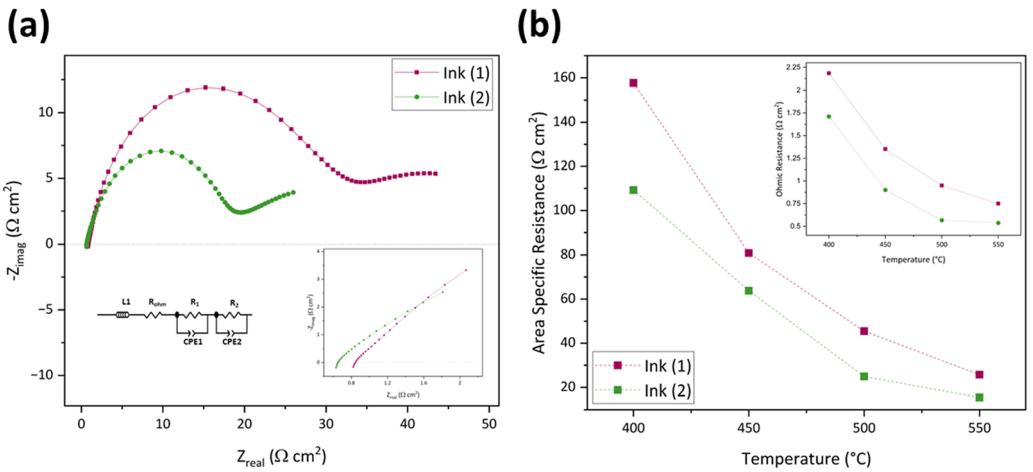

Fig. 5 (a) Comparison of the electrochemical performance of symmetric inkjet printed cells by Ink (1) and Ink (2) at 550 °C. The insets are the enlarged Nyquist plots of the higher frequency region (1.07–100 kHz) and the applied equivalent circuit. (b) ASR comparison of inkjet-printed symmetric cells with Ink (1) and Ink (2) from 400–550 °C. The inset is the comparison of R_{Ohm} of the as-mentioned cells in the same temperature range.

high frequencies, two depressed semi-circles, and an intermediate region. The equivalent circuit to fit the EIS data is shown in the inset of Fig. 6. L_1 is the measurement setup's inductance, mainly determined by the length of the measuring wires. The high-frequency intercept on the real axis demonstrates the ohmic resistance (R_{Ohm}), driven by the oxygen ion conduction in the electrolyte and electron transfer in the electrode and current collector.[75,76] Moreover, the high-frequency arc is the charge transfer mechanism linked to oxygen transport at the electrolyte/electrode contact area, demonstrated as R_1.[77] And R_2 features the low-frequency arc generated by the oxygen ion diffusion and adsorption/desorption on the electrode material's surface.[78] R_1 and R_2 show the electrode mechanisms in the cell associated with polarization resistance (R_p), which is smaller than the total of R_1 and R_2 since they overlap.[30]

The inset of Fig. 5(a) shows an enlarged image of the higher-frequency region (1.07–100 kHz) to provide a better picture of R_{Ohm} comparison. The ohmic resistance for the inkjet-printed cell with Ink (1) at 550 °C is 0.86 Ω cm^2, which is 36.38% higher than that of Ink (2) (0.53 Ω cm^2). This difference in R_{Ohm} can be attributed to different particle size distributions in Ink (1) and Ink (2). Ink (1) had a larger D50 with a secondary peak, which can cause poor dispersion of cathode active material in ink and affect the electrode/electrolyte interface due to the particle agglomeration and non-uniform structure and not providing good contact with the electrolyte.[79] In the case of the electrode process, Ink (2) possesses a lower R_1 compared to Ink (1) due to the better oxygen transport at the electrode/electrolyte interface. This enhancement arises from the narrow particle size distribution and smaller particle size compared to Ink (1), leading to a more homogenous microstructure with a higher specific surface area.[79,80] Also, R_2 is different in these two inks, as the particle size distribution impacts the gas diffusion properties of the electrode. Larger particles and secondary peaks of Ink (1) can cause agglomeration, block the active sites, and reduce the lengths of triple phase boundaries (TBPs). On the other hand, Ink (2)'s cell performance is better due to

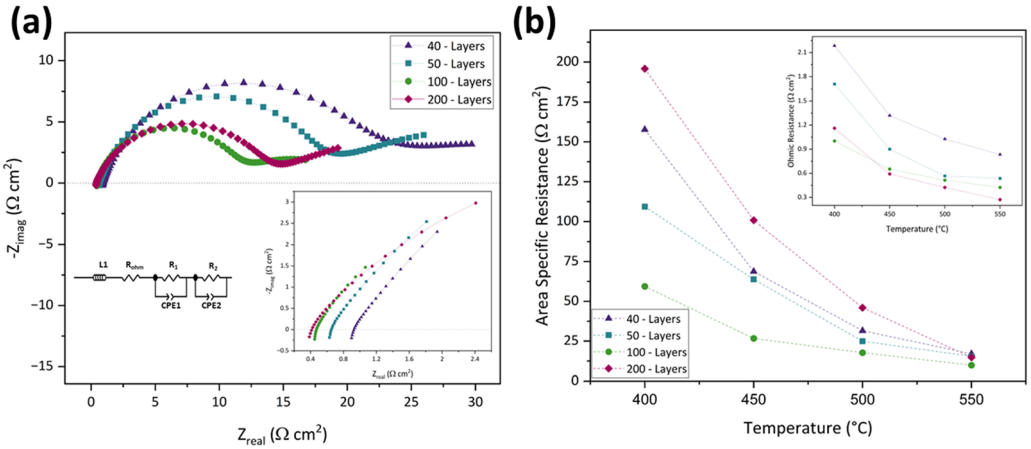

Fig. 6 (a) Comparison of the electrochemical performance of symmetric inkjet printed cells by Ink (1) and Ink (2) at 550 °C. The insets are the enlarged Nyquist plots of the higher frequency region (1.07–100 kHz) and the applied equivalent circuit. (b) ASR comparison of inkjet-printed symmetric cells with different numbers of printed layers, including 40-, 50-, 100-, and 200-layers, from 400–550 °C. The inset is the comparison of R_{Ohm} of the as-mentioned cells at the same temperature.

its more porous microstructure and increased TBP lengths.[74,80] Fig. 5(b) and its inset exhibit a comparison of area-specific resistance (ASR),[81] which is calculated by eqn (6), and the R_{Ohm} of inkjet-printed cells with Ink (1) and Ink (2) from 400–550 °C.

$$\text{Area} - \text{specific resistance} = \frac{R_1 + R_2}{2} - R_{Ohm} \qquad (6)$$

Table 2 represents the R_{Ohm}, R_1, R_2, and ASR for both inks.

The number of printed layers optimization. After finding the right ink, Ink (2), different numbers of layers, including 30, 40, 50, 100, and 200 layers, were inkjet-printed on the porous GDC–NLK pellets to optimize the inkjet printing conditions. All the samples were studied using the EIS technique to determine the best assembly, as the number of inkjet-printed lasers can affect the polarization resistance in some ways, including thickness and porosity.[79] Fig. 6(a) shows the Nyquist plots of inkjet-printed symmetric cells with 40, 50, 100, and 200 layers of Ink (2) at 550 °C. The insets are the expanded Nyquist plots for the as-mentioned samples in the higher frequency region (1.07–100 kHz) to provide a clearer image of the R_{Ohm}, and the applied equivalent circuit, respectively. It is also worth mentioning that the 30-layer symmetric cells didn't have a presentable performance.

According to the plots, the ASR decreased by increasing the number of printed layers, achieving the lowest value in the 100-layer inkjet-printed symmetric cell (9.91 Ω cm^2), and began to increase after that. This decrement until reaching 100 layers and then increasing behavior of R_p is attributable to the electrode layer's thickness and $CuFe_2O_4$ content.[82] In the 30-layer design, the electrode active material was insufficient and could not provide enough active sites for oxygen reduction. By increasing the number of inkjet-printed layers to 40 and 50, R_p decreased as the $CuFe_2O_4$ content and thickness increased by bringing more active areas for the electrode reactions. In the 100-layer case, R_p reached its optimum value as the electrode layer was thin enough to access and react with the electrolyte yet thick enough to offer adequate active sites for the reaction.[83] However, in the 200-layer case, the electrode layer was too high and became less porous, inhibiting the oxygen transfer and causing R_p increment.[83]

On the other hand, there is a different trend in R_{Ohm}. R_{Ohm} is inversely proportional to the number of inkjet-printed layers. This means that the 200-layer inkjet printed symmetric cell has the lowest R_{Ohm}, and the 40-layer one has the highest. The decreasing R_{Ohm} may be ascribed to the improved electrolyte/electrode interface due to the presence of more active material and better packing.[84] Fig. 6(b) and its inset illustrate the comparison of ASR and R_{Ohm} in 40-, 50-, 100-, and 200-layer inkjet printed symmetric cells in the 400–550 °C temperature range. Overall, the 100-layer inkjet-printed symmetric cell was chosen as the optimized cell due to its lowest ASR and reasonable R_{Ohm}. Table 3 presents the R_{Ohm}, R_1, R_2, and ASR of the 40-, 50-, 100-, and 200-layer inkjet-printed cells from 400–550 °C.

Table 2 R_{Ohm}, R_1, R_2, and ASR values of Ink (1) and Ink (2) inkjet-printed porous NLK–GDC symmetric cells in the 400–550 °C temperature range under an air atmosphere

	Ink (1) inkjet-printed cells (Ω cm^2)				Ink (2) inkjet-printed cells (Ω cm^2)			
Temperature (°C)	R_{Ohm}	R_1	R_2	ASR	R_{Ohm}	R_1	R_2	ASR
400	2.58	235.77	145.45	187.97	1.68	114.69	107.32	109.85
450	1.60	111.04	73.44	90.60	0.86	67.58	61.81	63.77
500	1.11	59.27	51.45	54.19	0.53	27.61	23.39	24.90
550	0.86	31.32	31.83	30.68	0.53	17.53	14.50	15.48

Table 3 R_{Ohm}, R_1, R_2, and ASR values of 40-, 50-, 100-, and 200-layer inkjet-printed porous NLK–GDC symmetric cells at 400–550 °C and under an air atmosphere

Cells	Resistance (Ω cm^2)	Temperature (°C) 400	450	500	550
40-Layers	R_{Ohm}	2.17	1.31	1.02	0.82
	R_1	197.80	74.47	37.52	19.09
	R_2	122.02	65.70	27.65	16.63
	ASR	157.70	68.73	31.54	17.04
50-Layers	R_{Ohm}	1.68	0.86	0.53	0.53
	R_1	114.69	67.58	27.62	17.53
	R_2	107.32	61.81	23.39	14.50
	ASR	109.28	63.77	24.90	15.48
100-Layers	R_{Ohm}	0.98	0.61	0.49	0.41
	R_1	62.59	29.41	19.09	10.32
	R_2	58.20	25.31	17.37	10.32
	ASR	59.39	26.71	17.69	9.91
200-Layers	R_{Ohm}	1.15	0.57	0.41	0.25
	R_1	212.38	131.03	19.87	17.74
	R_2	181.49	71.76	31.99	12.49
	ASR	195.75	100.80	45.96	14.83

Comparison of drop-cast and inkjet-printing techniques – For Ink (2). Once the printing conditions were tuned, the optimized inkjet-printed cell with 100 layers was compared to a drop-cast symmetric cell with the same ink to study the effect of the fabrication technique on electrochemical performance. Fig. 7(a) and (b) exhibit the electrochemical performance of drop-cast and 100-layer inkjet-printed symmetric cells at 400–550 °C under an air atmosphere, respectively. As mentioned before, the electrode microstructure significantly impacts the electrochemical performance and the ORR as the number of TBPs correlates with the gas adsorption and diffusion quantity, which are influenced by the electrode fabrication techniques.[85,86] Since inkjet-printing creates a hierarchical porous nanostructure and provides more reaction sites,[29,30] the inkjet-printed sample's ASR dropped to 9.91 Ω cm^2, 2.3 times lower than the drop-cast sample with 22.90 Ω cm^2 at 550 °C. This effect is visible in the arc radii of the low-frequency zone in the Nyquist plots of the as-mentioned samples in Fig. 7(c). Moreover, inkjet printing raises the electrode's specific surface area by homogenously spreading a notable number of nanoparticles on the electrolyte surface, improving the electrochemical performance and lowering ASR.

The electrode fabrication technique can also impact the R_{Ohm} as the charge transfers between the electrode and the electrolyte and, inversely, may be facilitated by a porous microstructure.[27,87,88] This is why the drop-cast symmetric cell

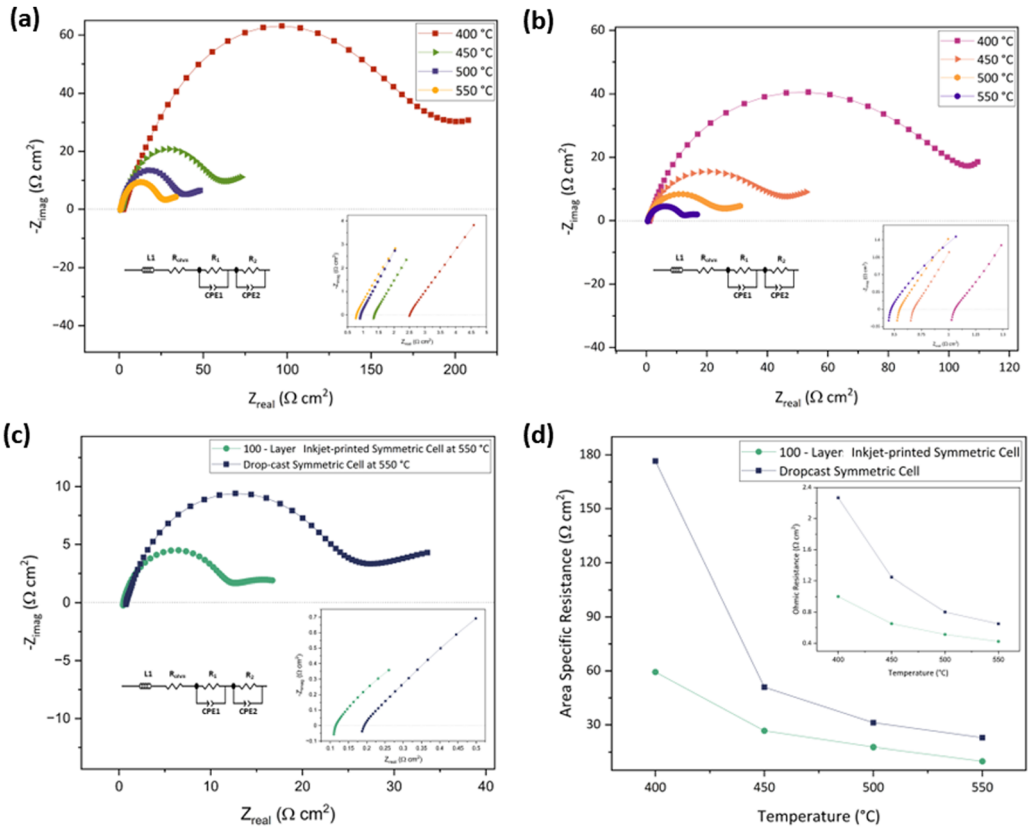

Fig. 7 The Nyquist plots of (a) drop-cast and (b) 100-layer inkjet-printed porous NLK–GDC symmetric cells with ink (2) at 400–550 °C under an air atmosphere. The insets are the enlarged Nyquist plots in the higher frequency zone (1.07–100 kHz) and the applied equivalent circuit. (c) Comparison of drop-cast and 100-layer inkjet-printed porous NLK–GDC symmetric cells with Ink (2) at 550 °C and the inset is the Nyquist plots in the higher frequency region (1.07–100 kHz). (d) ASR and R_{Ohm} (inset) comparison of drop-cast and 100-layer inkjet-printed porous NLK–GDC symmetric cells at 400–550 °C and under an air atmosphere.

Table 4 R_{Ohm}, R_1, R_2, and ASR values of the drop-cast and 100 layers inkjet-printed porous NLK–GDC symmetric cells with Ink (2) at 400–550 °C and under an air atmosphere

	Drop-cast cell (Ω cm^2)				100-layer inkjet-printed cell (Ω cm^2)			
Temperature (°C)	R_{Ohm}	R_1	R_2	ASR	R_{Ohm}	R_1	R_2	ASR
400	2.25	194.60	163.02	176.54	0.98	62.59	58.20	59.39
450	1.23	56.57	47.88	50.95	0.61	29.41	25.31	26.71
500	0.78	34.20	29.86	31.21	0.49	19.09	17.37	17.69
550	0.61	25.89	21.18	22.90	0.41	10.32	10.32	9.91

has a 1.5 times higher R_{Ohm} (0.61 Ω cm^2) than the 100-layer inkjet-printed sample (0.41 Ω cm^2) at 550 °C. A comparison of the ASR and R_{Ohm} of the drop-cast and 100-layer inkjet printed porous symmetric cells at 400–550 °C under an air atmosphere is given in Fig. 7(d) and its inset, respectively. The R_{Ohm}, R_1, R_2, and ASR of the drop-cast and 100-layer inkjet-printed samples are outlined in Table 4.

Comparison of drop-cast and inkjet-printing techniques – For Ink (2) – Samba. The electrochemical performance and Nyquist plots of the drop-cast and 100-layer inkjet-printed porous GDC–NLK with Ink (2) – Samba at 400–550 °C under an air atmosphere are shown in Fig. 8(a) and (b), respectively. Like Ink (2), the inkjet-printed symmetric cell performed much better than the drop-cast one by showing a 3.2 and 1.5 times lower ASR and R_{Ohm}, respectively. The electrochemical performance of Ink (2) – Samba was also superior to that of Ink (2), with ASR and R_{Ohm} values of 5.99 and 0.39 Ω cm^2, respectively, compared to 9.91 and 0.41 Ω cm^2 for Ink (2). The Ink (2) – Samba's reduced viscosity and narrower particle size distribution may be responsible for the advancement. Because of the increased surface area provided by the smaller particles, the number of reaction sites available to the electrode increases.[29,30]

In addition, the Samba cartridge has a higher drop placement accuracy, providing a more homogenous coating compared to the DMP cartridge.[89] The lower R_{Ohm} of Ink (2) – Samba can be attributable to the smaller particle size distribution which improved the electrode/electrolyte interface.[79]

Table 5 presents the R_{Ohm}, R_1, R_2, and ASR values of the drop-cast and 100-layer inkjet-printed samples with Ink (2) – Samba.

Comparison of *I–V* measurements for drop-cast and inkjet-printing techniques – Ink (2) – Samba. Fig. 9 displays the current–voltage (*I–V*) and current–power (*I–P*) curves of the

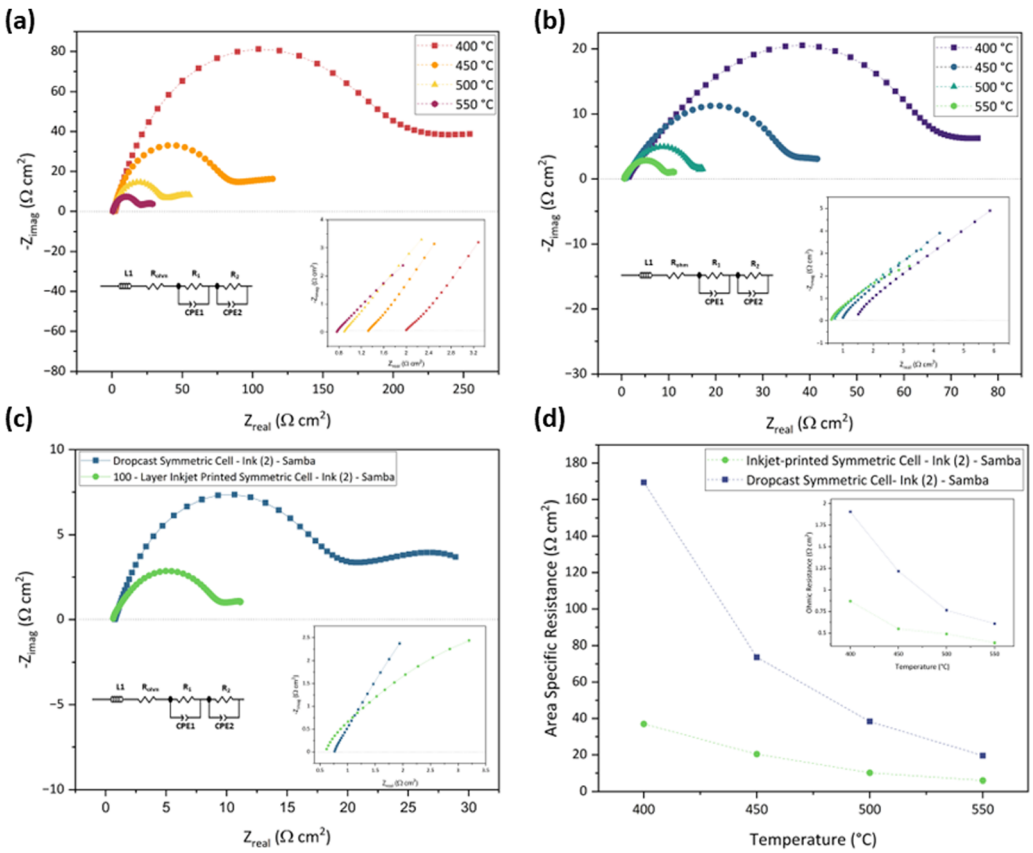

Fig. 8 The Nyquist plots of (a) drop-cast and (b) 100-layer inkjet-printed porous NLK–GDC symmetric cells with ink (2) – Samba at 400–550 °C under an air atmosphere. The insets are the enlarged Nyquist plots in the higher frequency zone (1.07–100 kHz) and the applied equivalent circuit. (c) Comparison of drop-cast and 100-layer inkjet-printed porous NLK–GDC symmetric cells with Ink (2) – Samba at 550 °C and the inset is the Nyquist plots in the higher frequency region (1.07–100 kHz). (d) ASR and R_{Ohm} (inset) comparison of drop-cast and 100-layer inkjet-printed porous NLK–GDC symmetric cells with Ink (2) – Samba at 400–550 °C and under an air atmosphere.

Table 5 R_{Ohm}, R_1, R_2, and ASR values of drop-cast and 100-layer inkjet-printed porous NLK–GDC symmetric cells with Ink (2) – Samba

Temperature (°C)	Drop-cast cell (Ω cm^2)				100-layer inkjet-printed cell (Ω cm^2)			
	R_{Ohm}	R_1	R_2	ASR	R_{Ohm}	R_1	R_2	ASR
400	1.90	174.00	168.60	169.39	0.87	48.96	26.78	37.00
450	1.21	80.55	69.15	73.63	0.55	23.21	18.74	20.42
500	0.76	48.01	30.19	38.33	0.49	12.72	8.53	10.13
550	0.60	25.15	15.25	19.59	0.39	7.37	5.39	5.99

anode-supported cells. It is important to acknowledge that the observed low open circuit voltage (OCV) and peak power density (PPD) values in both cells are influenced by the thick electrolyte and anode layer used. This thickness hinders efficient movement of ions inside the cell, ultimately leading to a low OCV.[90] The OCV values for 100-layer inkjet-printed and drop-cast samples are 0.95 V and 0.48 V at 650 °C, respectively. The increased open circuit voltage (OCV) observed in the inkjet-printed sample can be attributed to its more porous microstructure and larger specific surface area of the cathode. These characteristics enhance mass transfer at the cathode side by increasing the number of TBP sites.[91,92] The PPD value observed in the inkjet-printed sample is approximately seven times greater than that of the drop-cast sample. The difference can be ascribed to the tailored microstructure, reduced pore diameter, increased specific surface area, and greater number of TBP sites present in the inkjet-printed sample. Consequently, these factors contribute to enhanced ORRs.[93,94] The OCV and peak power density (PPD) values for different temperatures are given in Table 6.

Microstructural characterization

SEM. Microscopic analysis was conducted on 100-layer inkjet-printed and drop-cast porous NLK–GDC symmetric cells by Ink (2) to study the differences in fabrication techniques and their effects on the electrochemical performance of the cells. Fig. 10 includes the surface morphology of 100-layer inkjet-printed (a), (c) and (e) and drop-cast samples (b), (d) and (f) by Ink (2), presented in 185×, 687×, and 4.15× magnifications. Fig. 10(a), (c) and (e) reveal an adequate and homogenous distribution of $CuFe_2O_4$ particles on the surface of the inkjet-printed sample.[88,95] In contrast, the drop-cast sample suffers from a poor spread of the active material without uniform surface coverage. The higher magnification SEM images in Fig. 10(c) and (e) indicate that $CuFe_2O_4$ possesses a conjugated hierarchical morphology, essential for improving the charge transfer process.[30] Furthermore, the morphology that is formed through the inkjet-printing approach provides a favorable environment for the oxygen reduction reaction (ORR) to occur at the surface of the cathode.[96] The drop-cast sample surface morphology in Fig. 10(d) and (f), however, does not reflect any hierarchical or conjugated structure, which hinders the effective ORR activity at the cathode surface[86] The particle size

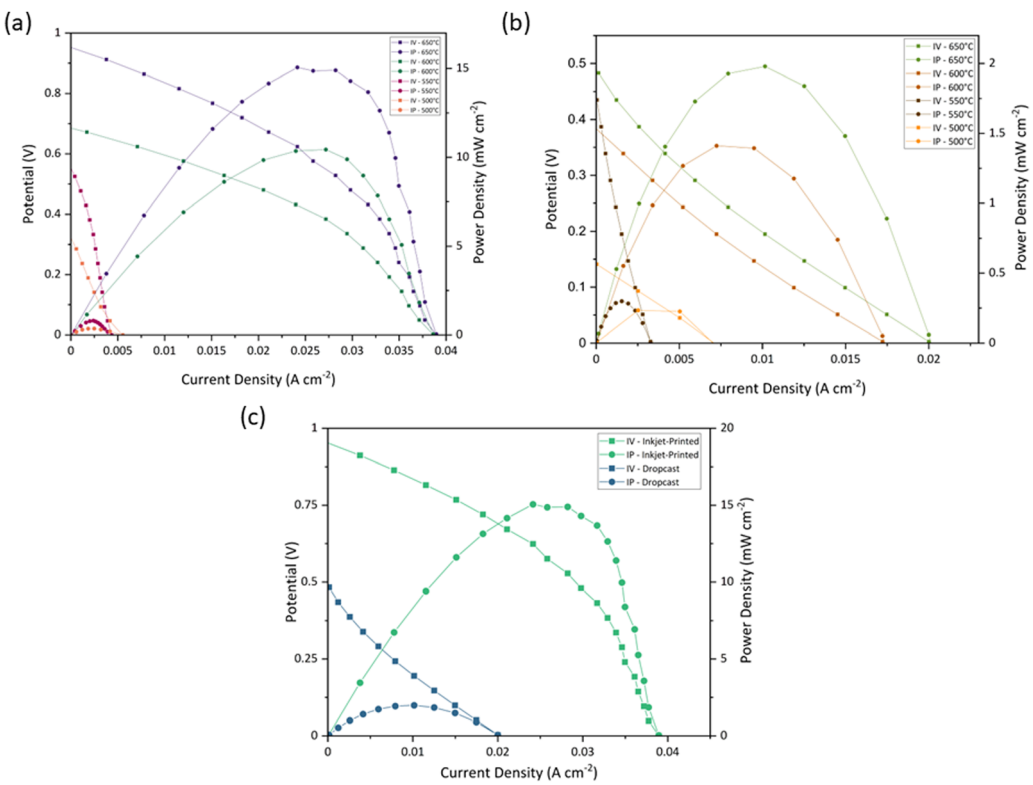

Fig. 9 IV and IP curves of (a) 100-layer inkjet-printed and (b) drop-cast full fuel cells with Ink (2) – Samba at 500–650 °C (H_2 with 5 L min^{-1} and air with 12.5 L min^{-1} were supplied on the anode and cathode sides, respectively), and (c) comparison of inkjet-printed and drop-cast full fuel cells with Ink (2) – Samba at 650 °C.

Table 6 OCV and PPD values for 100-layer inkjet-printed and drop-cast full fuel cells with Ink (2) – Samba at 500–650 °C (H_2 with 5 L min^{-1} and air with 12.5 L min^{-1} were supplied on the anode and cathode sides, respectively)

	PPD (mW cm^{-2})		OCV (V)	
Temperature (°C)	100-Layer inkjet-printed	Drop-cast	100-Layer inkjet-printed	Drop-cast
500	0.35	0.23	0.32	0.14
550	0.79	0.29	0.54	0.43
600	10.43	1.41	0.68	0.38
650	15.06	1.97	0.95	0.48

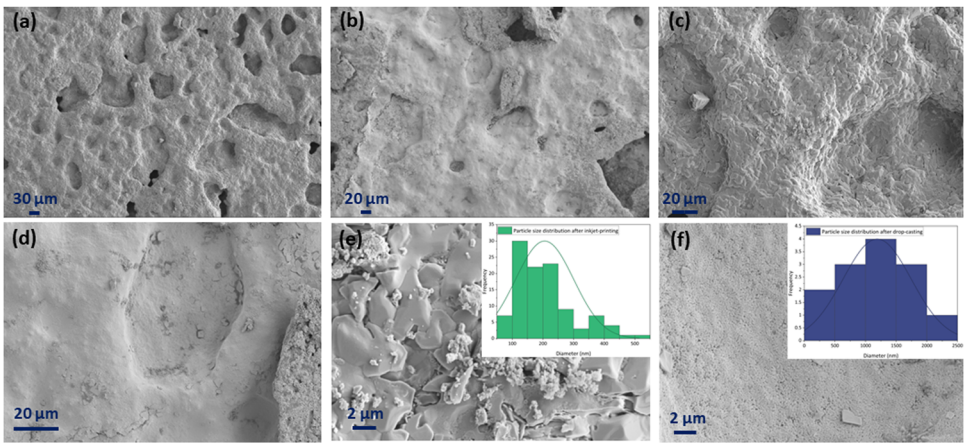

Fig. 10 Surface SEM images of (a), (c) and (e) 100-layer and (b), (d) and (f) drop-cast porous NLK–GDC symmetric cells in 185× (a and b), 687× (c and d), and 4.15k× (e and f) magnifications. The insets of (e) and (f) figures are the particle size distributions of $CuFe_2O_4$ particles on the surface of the inkjet-printed and drop-cast samples, respectively, analyzed using ImgaeJ software.

distribution of the samples, studied by ImageJ software, is presented in Fig. 10(e) and (f) for inkjet-printed and drop-cast samples, respectively. The results show that the average particle size in the inkjet-printed surface is 142 nm in diameter, which is much smaller than that of the drop-cast sample, 1161 nm. This study can confirm the EIS results as the inkjet-printed cell provides a higher specific surface area for surface reactions and increases the reaction sites.[29,97,98] Moreover, it indicates that the inkjet-printing fabrication technique can potentially reduce the particle size distribution during the deposition due to its high-velocity ink ejection.

A high-magnification SEM image of the inkjet printed sample is shown in Fig. 11(a) to provide a better picture of this homogenous spread of the nanoparticles on the surface. The particle size distribution of this image is also studied by ImageJ software, displayed in Fig. 11(b), and it was 57 nm in diameter.

Fig. 12 displays the cross-sectional view in the interface area of the inkjet-printed and drop-cast samples in (a), (c), (e) and (b), (d), (f) with different magnifications, respectively. The electrode/electrolyte interface is crucial to SOFC performance as it affects electrode and electrolyte contact and increases active reaction sites, and therefore its research is essential.[99–101]

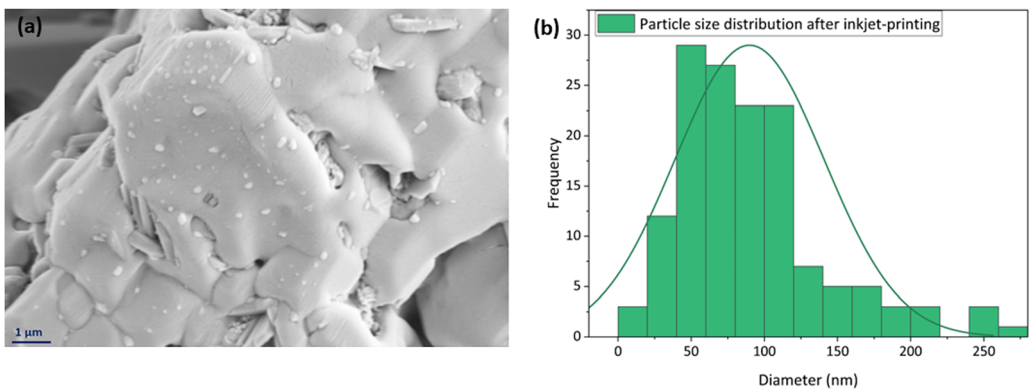

Fig. 11 (a) Surface SEM image with a high magnification of 8.66k× from the 100-layer inkjet-printed sample and (b) $CuFe_2O_4$ nanoparticle size distribution on its surface, analyzed using ImageJ software.

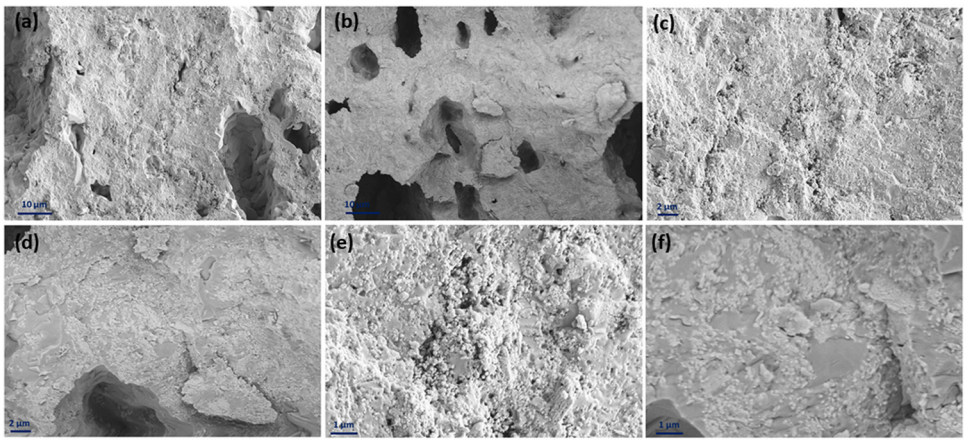

Fig. 12 Cross-sectional SEM images of (a), (c) and (e) 100-layers and (b), (d) and (f) drop-cast porous NLK–GDC symmetric cells in 1.23k× (a and b), 3.71k× (c and d), and 9.77k× (e and f) magnifications.

From Fig. 12, especially in the higher magnification images of Fig. 12(c) and (e), it can be seen that the inkjet-printed sample electrode/electrolyte interface is fully covered with the $CuFe_2O_4$ nanoparticles, showing favorable ink infiltration to the substrate's porous layer. However, the interface area for the drop-cast sample is more like scattered islands of the agglomerated $CuFe_2O_4$ nanoparticles. These observations align with the enhanced electrochemical performance of the inkjet-printed samples because of the electrode/electrolyte interface improvement by emerging $CuFe_2O_4$ nanoparticles and providing more triple-phase boundaries.[30,102] The electrode/electrolyte interface behavior happened for the symmetric cells coated with Ink (2) – Samba. The interface area is shown in Fig. 13(a), (c), (b) and (d) for the inkjet-printed and drop-cast porous NLK–GDC symmetric cells by Ink (2) – Samba, respectively. Comparing the lower magnification SEM images in Fig. 13(a) and (b), it is clear that the inkjet-printing technique was more successful in spreading the $CuFe_2O_4$ nanoparticles along the interfacial area as there are only some scattered particles in the drop-cast one. Fig. 13(c) exhibits effective ink penetration through the porous layer, while the drop-cast cells in Fig. 13(d) have aggregated islands of $CuFe_2O_4$ nanoparticles.

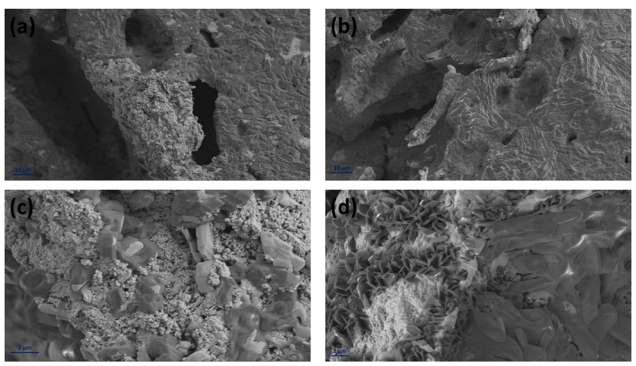

Fig. 13 Cross-sectional SEM images of (a) and (c) 100-layer and (b) and (d) drop-cast porous NLK–GDC symmetric cells by Ink (2) – Samba in 787× (a and b) and 5.33k× (c and d) magnifications.

Table 7 BET results for 100-layer inkjet-printed and drop-cast porous NLK–GDC symmetric cells with Ink (2) – Samba

Samples	Specific surface area ($m^2\ g^{-1}$)	Mean pore diameter (nm)
100-Layer inkjet-printed	2.25	19.12
Drop-cast	1.84	22.51

BET. Table 7 displays the specific surface area and mean pore diameter of 100-layer inkjet-printed and drop-cast porous NLK–GDC symmetric cells with Ink (2) – Samba. The acquired data aligns with the initial expectations and corresponds with the broader framework of our research, highlighting the enhanced role of inkjet-printing in enhancing the specific surface area. This, in turn, results in the formation of a hierarchical surface microstructure in the cathode material, which boosts the electrochemical performance through the creation of additional reaction sites.

Conclusion

$CuFe_2O_4$ ink for inkjet-printing fabrication techniques was developed for the first time by optimizing the 1,5-pentandiol wt% as the dispersant. Three inks with 0, 15, and 20 wt% 1,5-pentandiol were prepared, and their particle size, viscosity, surface tension, and density were studied to determine the best ink for inkjet printing. Although all three inks were theoretically printable according to their Z values, Ink (1) and Ink (2) were selected because of their smaller particle sizes (D50 of 1.26, and 0.87 μm, respectively) and higher stability. To choose the best ink for SOFC application, porous NLK–GDC pellets were inkjet printed with 50 layers of Ink (1) and Ink (2) to fabricate symmetric cells for EIS analysis at 400–550 °C and under an air atmosphere. Inkjet-printed cells with Ink (2) performed better by showing 1.7 and 2 times lower R_{Ohm} and ASR than Ink (1) cells, as Ink (2) had a smaller particle size, which created a more homogeneous porous microstructure and enhanced the gas transfers. Then, Ink (2) was picked to

optimize the inkjet-printing conditions by changing the number of inkjet-printed layers. Porous NLK–GDC were inkjet-printed by 30, 40, 50, 100, and 200 layers of Ink (2). Among them, the 100-layer inkjet-printed symmetric cell had the best performance with an ASR of 9.91 Ω cm^2 because the electrode layer was thin enough to access and react with the electrolyte yet thick enough to supply appropriate active sites for the reaction. Then, the 100-layer inkjet-printed symmetric cell with Ink (2) was compared with a drop-cast symmetric cell with the same ink using an EIS technique to study the effect of the fabrication technique on the cell performance. The inkjet printing technique lowered the ASR from 22.90 to 9.91 Ω cm^2 by creating a hierarchical porous microstructure and optimizing the reaction sites. Next, Ink (2) was modified for the Samba cartridge by regulating its viscosity with cyclopentanone, and the same procedure was done for the Ink (2) – Samba. The values of D50 and *Z* parameter for the modified ink were 0.68 μm and 3.89, respectively. The electrochemical performance comparison of the drop-cast and 100-layer inkjet-printed symmetric cells with Ink (2) – Samba showed a reduction in the ASR value from 19.59 to 5.99 Ω cm^2 owing to the surface modification by the inkjet-printing technique which has direct effects on the cathode ORR. Finally, Ink (2) – Samba was used to fabricate anode-supported full fuel cells by inkjet-printing and drop-cast techniques. The 100-layer inkjet-printed sample presented 15.06 mW cm^{-2}, which is 7 times higher than that of the drop-cast one, 1.97 mW cm^{-2}. These findings imply that the manufacturing process can considerably impact the quality of an electrode and its electrochemical performance in a fuel cell. For manufacturing sophisticated low-temperature ceramic fuel cells, inkjet printing, which can provide a better electrolyte/electrode interface and triple-phase boundary length, has the potential to surpass current fuel cell fabrication technologies.

Author contributions

Sanaz Zarabi Golkhatmi: conceptualization, methodology, investigation, formal analysis, validation, visualization, writing – original draft, revision. Muhammad Imran Asghar: conceptualization, methodology, investigation, formal analysis, validation, visualization, editing – original draft, revision, funding, supervision. Peter D. Lund: editing – original draft, supervision.

Conflicts of interest

There are no conflicts to declare.

Acknowledgements

The authors thank Academy of Finland (Grant No. 13329016, 13322738, 13352669) for their financial support. The Academy of Finland's RawMatTERS Finland Infrastructure (RAMI) at Aalto University was utilized in this research.

References

1 J. Li, L. Fan, N. Hou, Y. Zhao and Y. Li, *RSC Adv.*, 2022, **12**, 13220–13227.
2 S. Hu, J. Li, Y. Zeng, J. Pu and B. Chi, *Phys. Chem. Chem. Phys.*, 2023, **25**, 5926–5941.
3 S. Sharma, P. Jakhar and H. Sharma, *J. Chin. Chem. Soc.*, 2023, **70**(2), 107.
4 A. Maleki, Z. Hajizadeh and P. Salehi, *Sci. Rep.*, 2019, **9**, 1–8.
5 C. Liu, B. Ma, Z. Lin, Y. Zhou and K. Wu, *Mater. Lett.*, 2022, **325**, 132860.
6 A. K. Ghasemi, M. Ghorbani, M. S. Lashkenari and N. Nasiri, *Electrochim. Acta*, 2023, **439**, 141685.
7 E. da, N. Silva, I. L. O. Brasileiro, V. S. Madeira, B. A. de Farias, M. L. A. Ramalho, E. Rodríguez-Aguado and E. Rodríguez-Castellón, *J. Environ. Chem. Eng.*, 2020, **8**, 104132.
8 M. Faheem, X. Jiang, L. Wang and J. Shen, *RSC Adv.*, 2018, **8**, 5740–5748.
9 C. Karthikeyan, K. Ramachandran, S. Sheet, D. J. Yoo, Y. S. Lee, Y. Satish Kumar, A. R. Kim and G. Gnana Kumar, *ACS Sustainable Chem. Eng.*, 2017, **5**, 4897–4905.
10 E. Ranjith Kumar, R. Jayaprakash, G. Sarala Devi and P. Siva Prasada Reddy, *Sens. Actuators, B*, 2014, **191**, 186–191.
11 M. A. Haija, G. Basina, F. Banat and A. I. Ayesh, *Mater. Sci. Pol.*, 2019, **37**, 289–295.
12 S. A. Soomro, I. H. Gul, H. Naseer, S. Marwat and M. Mujahid, *Curr. Nanosci.*, 2019, **15**, 420–429.
13 L. Luo, R. Cui, H. Qiao, K. Chen, Y. Fei, D. Li, Z. Pang, K. Liu and Q. Wei, *Electrochim. Acta*, 2014, **144**, 85–91.
14 M. Israr, J. Iqbal, A. Arshad, A. Sadaf, M. Rani, M. Rani and S. Jabeen, *J. Phys. D: Appl. Phys.*, 2021, **54**, 395501.
15 M. Chandel, D. Moitra, P. Makkar, H. Sinha, H. S. Hora and N. N. Ghosh, *RSC Adv.*, 2018, **8**, 27725–27739.
16 B. Saravanakumar, S. P. Ramachandran, G. Ravi, V. Ganesh, R. K. Guduru and R. Yuvakkumar, *Vacuum*, 2019, **168**, 108798.
17 S. N. Hosseini, F. Karimzadeh, M. H. Enayati and N. M. Sammes, *Solid State Ionics*, 2016, **289**, 95–105.
18 Y. Liu, Y. Wu, W. Zhang, J. Zhang, B. Wang, C. Xia, M. Afzal, J. Li, M. Singh and B. Zhu, *Int. J. Hydrogen Energy*, 2017, **42**, 17514–17521.
19 M. I. Asghar, X. Yao, S. Jouttijärvi, E. Hochreiner, R. Virta and P. D. Lund, *Int. J. Hydrogen Energy*, 2020, **45**, 24083–24092.
20 M. A. S. Amulya, H. P. Nagaswarupa, M. R. A. Kumar, C. R. Ravikumar, K. B. Kusuma and S. C. Prashantha, *J. Phys. Chem. Solids*, 2021, **148**, 109756.
21 C. Karunakaran, S. SakthiRaadha, P. Gomathisankar and P. Vinayagamoorthy, *RSC Adv.*, 2013, **3**, 16728–16738.
22 S. Hariganesh, S. Vadivel, B. paul, M. Kumaravel, N. Balasubramanian, S. Rajendran and S. Sankar Dhar, *Inorg. Chem. Commun.*, 2021, **125**, 108405.
23 A. M. Sukeshini, R. Cummins, T. L. Reitz and R. M. Miller, *Electrochem. Solid State Lett.*, 2009, **12**, B176.

24 L. Zouridi, I. Garagounis, A. Vourros, G. E. Marnellos and V. Binas, *Adv. Mater. Technol.*, 2022, **7**, 2101491.
25 L. J. Deiner and T. L. Reitz, *Adv. Eng. Mater.*, 2017, **19**, 1600878.
26 A. Teichler, J. Perelaer and U. S. Schubert, *J. Mater. Chem. C*, 2013, **1**, 1910–1925.
27 O. Rahumi, A. Sobolev, M. K. Rath and K. Borodianskiy, *J. Eur. Ceram. Soc.*, 2021, **41**, 4528–4536.
28 V. Esposito, C. Gadea, J. Hjelm, D. Marani, Q. Hu, K. Agersted, S. Ramousse and S. H. Jensen, *J. Power Sources*, 2015, **273**, 89–95.
29 G. D. Han, K. Bae, E. H. Kang, H. J. Choi and J. H. Shim, *ACS Energy Lett.*, 2020, **5**, 1586–1592.
30 S. Z. Golkhatmi, M. I. Asghar and P. D. Lund, *J. Power Sources*, 2022, **552**, 232263.
31 A. Kushwaha, M. K. Jangid, B. B. Bhatt, A. Mukhopadhyay and D. Gupta, *ACS Appl. Energy Mater.*, 2021, **4**, 7911–7921.
32 Y. Gu, A. Wu, H. Sohn, C. Nicoletti, Z. Iqbal and J. F. Federici, *J. Manuf. Process.*, 2015, **20**, 198–205.
33 S. Lawes, Q. Sun, A. Lushington, B. Xiao, Y. Liu and X. Sun, *Nano Energy*, 2017, **36**, 313–321.
34 A. Sajedi-Moghaddam, M. Gholami and N. Naseri, *ACS Appl. Mater. Interfaces*, 2023, **15**(3), 3894–3903.
35 K.-H. Choi, J. Yoo, C. K. Lee and S.-Y. Lee, *Energy Environ. Sci.*, 2016, **9**, 2812–2821.
36 S. S. Delekta, A. D. Smith, J. Li and M. Östling, *Nanoscale*, 2017, **9**, 6998–7005.
37 A. Singh, M. Katiyar and A. Garg, *RSC Adv.*, 2015, **5**, 78677–78685.
38 S. Jung, A. Sou, K. Banger, D. Ko, P. C. Y. Chow, C. R. McNeill and H. Sirringhaus, *Adv. Energy Mater.*, 2014, **4**, 1400432.
39 T. M. Eggenhuisen, Y. Galagan, A. Biezemans, T. Slaats, W. P. Voorthuijzen, S. Kommeren, S. Shanmugam, J. P. Teunissen, A. Hadipour and W. J. H. Verhees, *J. Mater. Chem. A*, 2015, **3**, 7255–7262.
40 T. Roberts, J. B. De Graaf, C. Nicol, T. Hervé, M. Fiocchi and S. Sanaur, *Adv. Healthcare Mater.*, 2016, **5**, 1462–1470.
41 F. J. Pavinatto, C. W. A. Paschoal and A. C. Arias, *Biosens. Bioelectron.*, 2015, **67**, 553–559.
42 D. D. Le, T. N. N. Nguyen, D. C. T. Doan, T. M. D. Dang and M. C. Dang, *Adv. Nat. Sci.: Nanosci. Nanotechnol.*, 2016, **7**, 25002.
43 R. I. Tomov, T. Mitchell-Williams, C. Gao, R. V. Kumar and B. A. Glowacki, *J. Appl. Electrochem.*, 2017, **47**, 641–651.
44 B. Derby, *Annu. Rev. Mater. Res.*, 2010, **40**, 395–414.
45 L. Nayak, S. Mohanty, S. K. Nayak and A. Ramadoss, *J. Mater. Chem. C*, 2019, **7**, 8771–8795.
46 R. I. Tomov, M. Dudek, S. C. Hopkins, M. Krauz, H. Wang, C. Wang, Y. Shi, P. Tomczyk and B. A. Glowacki, *ECS Trans.*, 2013, **57**, 1359.
47 I. Kim, S. Kim, A. Andreu, J.-H. Kim and Y.-J. Yoon, *Addit. Manuf.*, 2022, **52**, 102659.
48 A. Kockmann, J. C. Porsiel, R. Saadat and G. Garnweitner, *RSC Adv.*, 2018, **8**, 11109–11118.
49 W. J. Tseng and K.-H. Teng, *Mater. Sci. Eng., A*, 2001, **318**, 102–110.
50 G. D. Han, H. J. Choi, K. Bae, H. R. Choi, D. Y. Jang and J. H. Shim, *ACS Appl. Mater. Interfaces*, 2017, **9**, 39347–39356.
51 G. D. Han, K. C. Neoh, K. Bae, H. J. Choi, S. W. Park, J.-W. Son and J. H. Shim, *J. Power Sources*, 2016, **306**, 503–509.
52 T. D. Grant, A. C. Hourd, S. Zolotovskaya, J. B. Lowe, R. J. Rothwell, T. D. A. Jones and A. Abdolvand, *Mater. Des.*, 2022, **214**, 110377.
53 A. Lesch, F. Cortés-Salazar, V. C. Bassetto, V. Amstutz and H. H. Girault, *Chim. Int. J. Chem.*, 2015, **69**, 284–289.
54 M. Zeng and Y. Zhang, *J. Mater. Chem. A*, 2019, **7**, 23301–23336.
55 G. Czechowski, A. Rabiega and J. Jadzyn, *Zeitschrift für Naturforsch. A*, 2003, **58**, 569–572.
56 K. Venkatramanan and V. Arumugam, *Int. J. Thermophys.*, 2006, **27**, 66–78.
57 R. Ben Haj-Kacem, N. Ouerfelli and J. V. Herráez, *Phys. Chem. Liq.*, 2015, **53**, 776–784.
58 R. Hamdi and E. Mliki, *South African J. Chem. Eng.*, 2023, **43**, 337–341.
59 J. Li, C. Zhang and J. Luo, *Langmuir*, 2013, **29**, 5239–5245.
60 M. U. Jewel, F. Mokhtari-Koushyar, R. T. Chen and M. Y. Chen, in 2018 IEEE 18th International Conference on Nanotechnology (IEEE-NANO), IEEE, 2018, pp. 1–4.
61 R. Balaji, M. Gowri Sankar, M. Chandra Sekhar and M. Chandra Shekar, *Phys. Chem. Liq.*, 2016, **54**, 422–439.
62 V. L. D. Costa, A. P. Costa and R. M. S. Simões, *Bio-Resources*, 2019, **14**, 7636–7654.
63 L. Ren, X. Luo and H. Zhou, *J. Am. Ceram. Soc.*, 2018, **101**, 3874–3889.
64 Z. Tang, K. Fang, M. N. Bukhari, Y. Song and K. Zhang, *Langmuir*, 2020, **36**, 9481–9488.
65 J. E. Fromm, *IBM J. Res. Dev.*, 1984, **28**, 322–333.
66 B. Derby, *J. Eur. Ceram. Soc.*, 2011, **31**, 2543–2550.
67 J. Zhang, Y. Cui and H. Wang, *J. Renewable Sustainable Energy*, 2013, **5**, 23117.
68 M. Zhang, H. Wang, F. Xiang and X. Yao, *Int. J. Appl. Ceram. Technol.*, 2009, **6**, 257–263.
69 D. Graf, A. Qazzazie and T. Hanemann, *Materials*, 2020, **13**, 2587.
70 H. Yuan, J. Liu, M. Gu, S. Feng, M. Zhou and Y. Luo, *Ceram. Int.*, 2021, **47**, 16641–16651.
71 X. Liu, W. Liu, C. Wang, Z. Zheng and L. Kong, *J. Electron. Mater.*, 2016, **45**, 5436–5442.
72 Z. Chen, J. Ouyang, W. Liang, Z. Yan, F. Stadler and C. Lao, *Ceram. Int.*, 2018, **44**, 13381–13388.
73 A. M. Balagurov, I. A. Bobrikov, M. S. Maschenko, D. Sangaa and V. G. Simkin, *Crystallogr. Rep.*, 2013, **58**, 710–717.
74 J. Cao, Y. Ji and Z. Shao, *Energy Environ. Sci.*, 2022, **15**, 2200–2232.
75 M. Zhiani, S. Majidi, V. B. Silva and H. Gharibi, *Energy*, 2016, **97**, 560–567.
76 J. Zhang, J. Wu, H. Zhang and J. Zhang, *PEM fuel cell testing and diagnosis*, Newnes, 2013.

77 M. B. Hanif, J.-T. Gao, K. Shaheen, Y.-P. Wang, M. Yasir, S.-L. Zhang, C.-J. Li and C.-X. Li, *J. Power Sources*, 2020, **472**, 228498.
78 D. M. Bastidas, S. Tao and J. T. S. Irvine, *J. Mater. Chem.*, 2006, **16**, 1603–1605.
79 K. Sasaki, J. Wurth, R. Gschwend, M. Gödickemeier and L. J. Gauckler, *J. Electrochem. Soc.*, 1996, **143**, 530.
80 M. J. Jørgensen and M. Mogensen, *J. Electrochem. Soc.*, 2001, **148**, A433.
81 G. Dong, C. Yang, F. He, Y. Jiang, C. Ren, Y. Gan, M. Lee and X. Xue, *RSC Adv.*, 2017, **7**, 22649–22661.
82 S. H. Chan, X. J. Chen and K. A. Khor, *J. Electrochem. Soc.*, 2003, **151**, A164.
83 Z. Lu, J. Hardy, J. Templeton and J. Stevenson, *J. Power Sources*, 2012, **198**, 90–94.
84 R. K. Sharma, M. Burriel, L. Dessemond, V. Martin, J.-M. Bassat and E. Djurado, *J. Power Sources*, 2016, **316**, 17–28.
85 S. B. Adler, *Chem. Rev.*, 2004, **104**, 4791–4844.
86 J. Parbey, Q. Wang, J. Lei, M. Espinoza-Andaluz, F. Hao, Y. Xiang, T. Li and M. Andersson, *Int. J. Hydrogen Energy*, 2020, **45**, 6949–6957.
87 A. Sánchez-Ruiz, A. Sousa-Hervés, J. C. Pérez-Flores, J. R. Marín-Rueda, J. Tolosa, A. Garzón-Ruiz, J. Rodríguez-López, J. Canales-Vázquez and J. C. García-Martínez, *Prog. Org. Coatings*, 2022, **166**, 106787.
88 C. Li, H. Chen, H. Shi, M. O. Tade and Z. Shao, *J. Power Sources*, 2015, **273**, 465–471.
89 T. Horter, H. Ruehl, W. Yang, Y.-S. Chiang, K. Glaeser and A. Zimmermann, *J. Manuf. Mater. Process.*, 2023, **7**, 20.
90 K. L. Duncan, K.-T. Lee and E. D. Wachsman, *J. Power Sources*, 2011, **196**, 2445–2451.
91 A. Seong, J. Kim, J. Kim, S. Kim, S. Sengodan, J. Shin and G. Kim, *J. Electrochem. Soc.*, 2018, **165**, F1098.
92 M. B. Hanif, J.-T. Gao, S. qayyum, K. Shaheen, Y.-P. Wang, M. Yasir, C.-J. Li and C.-X. Li, *Ceram. Int.*, 2021, **47**, 10893–10904.
93 J. Deseure, Y. Bultel, L. Dessemond and E. Siebert, *Electrochim. Acta*, 2005, **50**, 2037–2046.
94 W. Chang, E. H. Kang, H. J. Jeong, W. Choi and J. H. Shim, *Energy*, 2023, **268**, 126489.
95 C. Wang, S. C. Hopkins, R. I. Tomov, R. V. Kumar and B. A. Glowacki, *J. Eur. Ceram. Soc.*, 2012, **32**, 2317–2324.
96 W. Zhang, H. Wang, K. Guan, Z. Wei, X. Zhang, J. Meng, X. Liu and J. Meng, *ACS Appl. Mater. Interfaces*, 2019, **11**, 26830–26841.
97 M. Ahn, J. Lee and W. Lee, *J. Power Sources*, 2017, **353**, 176–182.
98 S. V. Jouttijärvi, M. I. Asghar and P. D. Lund, *Catal. Today*, 2021, **364**, 104–110.
99 J. A. Cebollero, R. Lahoz, M. A. Laguna-Bercero and A. Larrea, *J. Power Sources*, 2017, **360**, 336–344.
100 H. Seo, H. Iwai, M. Kishimoto, C. Ding, M. Saito and H. Yoshida, *J. Power Sources*, 2020, **450**, 227682.
101 C. Lee, S. S. Shin, J. Kim, J. Choi, M. Choi and H. H. Shin, *ACS Appl. Mater. Interfaces*, 2022, **14**, 32124–32133.
102 L. Bi, S. P. Shafi, E. H. Da'as and E. Traversa, *Small*, 2018, **14**, 1801231.